Cross-sectional optimization of whispering-gallery mode sensor with high electric field intensity in the detection domain

Akihiro Takezawa, *Member, IEEE,* Masanobu Haraguchi, Toshihiro Okamoto and Mitsuru Kitamura

***Abstract*—Optimal cross-sectional shapes for whispering-gallery mode sensors with prescribed emission wavelengths and resonance modes are generated through topology optimization based on the finite element method. The sensor is assumed to detect the state of the domain surrounded by the sensor. We identified the integral of the square of the electric field intensity over the detection domain and the quality factor (Q factor), which should be maximized, as key values for the sensor sensitivity, representing the detection limit for the relative permittivity change of the test object. Based on this, the integral of the square of the electric field intensity over the detection domain and the Q factor are studied as the optimization targets. In our numerical study, their optimal configuration characteristics are identified and analyzed. The resulting device has a small radius, a small detection domain and a concave shape with a center located next to the detection domain. We also succeeded in performing simultaneous optimization of the integral of the square of the electric field intensity over the detection domain and the Q factor.**

I. Introduction

Micro-ring resonators with whispering-gallery mode (WGM) resonance have tremendous potential for applications in optics [1], [2]. The WGM, which is set up in these devices by emissions from the input light, forms circular continuous closed beams governed by internal reflections along the resonator boundary. Because the light wave is trapped within a very small volume during WGM emission, a high quality factor (Q factor) can be achieved in WGM devices.

Since the behavior of the trapped light is very sensitive to changes in the device's shape or surroundings, the use of the WGM resonator as a sensor was studied. These sensors have been used to detect the condition of a surrounding liquid [3], [4], [5], [6], temperature [7], force [8], pressure [9] and the condition of composite materials [10]. The representative example used here is label-free bio-sensing. The optical path in the WGM device can be changed even by the binding of molecules. The variation in the optical path can be detected as a shift in the resonance wavelength [3], [5].

In this research, to enhance the detection performance for the state of a surrounding liquid, a sensor for a specified domain state is considered, such as a density sensor. In the conventional WGM sensor, sphere, toroidal, ring or disk shapes are used for ease of manufacturability. However, because these shapes cover the energy hot spot of the WGM, better shapes could exist for sensing applications. Although it may cause the Q factor to decrease, a shape that reveals the WGM hot spot to the sensing domain is preferable for the sensor. Apart from their manufacturability, the study of these shapes also contributes to the WGM sensor device development.

The search for a novel device geometry can be assisted by accurate numerical performance analysis. The WGM is usually evaluated through an eigenvalue analysis based on the finite-element method (FEM). In particular, because of the circular shape of the device and the optical mode, axisymmetric models are effective for simulation of the WG resonance mode in ring resonators. The relevant details are explained in [11]. Although the FEM has been used before to analyze the electric field behavior from the top view of the WGM [12], few detailed numerical studies of the cross-section of the WGM sensor have previously been performed. Moreover, because variation in the device shape causes variation in the resulting WGM order and emission wavelength, a detailed search for an optimal device shape for a specified wavelength can be quite challenging. Thus, detailed shape optimization provides a means to develop high performance devices that would be available for a wide variety of applications.

Topology optimization [13] has previously contributed to the optimal design of novel optical devices [14], [15], [16], [17], [18]. In this approach, the designed devices are represented by distributions of the dielectric materials or metals in the analysis model. By updating these distributions using a gradient-based optimization method, the generated distribution represents the shapes of devices that attain specific performance criteria. In previous research, the authors have applied topology optimization to the optimization of the fundamental characteristics of the WGM resonator, maximization of the Q factor and minimization of the mode volume [19].

In this research, we study and identify the optimal shapes for WGM sensors using FEM-based topology optimization. This systematic procedure helps us to find optimal device shapes with fixed design performance for a prescribed emission wavelength and WG resonance mode. A sensor sensitivity criterion, representing the detection limit of the relative permittivity change of the test object, is first formulated using the integral of the square of the electric field intensity over

A. Takezawa and M. Kitamura are with the Institute of Engineering, Hiroshima University, Higashi-Hiroshima, Hiroshima 739-8527, Japan (corresponding author, A. Takezawa; phone: +81-82-424-7544; fax: +81-82-422-7194; e-mail: akihiro@hiroshima-u.ac.jp).

M. Haraguchi and T. Okamoto are with the Institute of Technology and Science, The University of Tokushima, Japan.

the detection domain and the Q factor. The analysis domains and the equations of state for the WGM ring resonators are then considered. Studies of the cross-sectional shapes of the WGM sensor are performed to formulate the optimization problem on the basis of the proposed criteria. The integral of the square of the electric field intensity over the detection domain and the Q factor are then formulated as objective functions, while the emission wavelength is formulated as an equality constraint. The proposed geometrical optimization is implemented as an optimization of the dielectric material distribution using the phase field method [20]. The optimization algorithm is constructed based on two-step FEM, sensitivity analysis of each objective function and density function constraint, and sequential linear programming (SLP). Finally, numerical examples are provided for validation of the proposed methodology. First, the effects of the size and location of the detection domain on the sensor performance are studied. Then, the simultaneous optimization of the integral of the square of the electric field intensity over the detection domain and the Q factor is considered.

II. Problem Settings

A. Design target and performance criteria

Using cylindrical coordinates, we model a WGM ring resonator centered on the origin in free space Ω, as shown in Fig. 1. The coordinate system is composed of the components (z, ϕ, r), which denote the axial, azimuthal and radial coordinates, respectively. A toroidal detection domain Ω_{det}, which is used to test a state of a liquid, such as its density, within the domain is also set in the cylindrical domain around the resonator. The vertical cross-sectional shape of the device in a specified domain that does not include Ω_{det} in the z-r plane is treated as the design target; we obtain the final axisymmetric form by generating the corresponding solid of revolution.

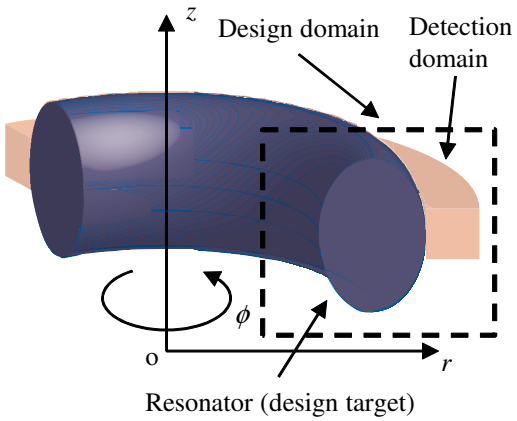

Fig. 1. The analysis and design domain as described in cylindrical coordinates. The purple toroid indicates the cross-sectional resonator shape that is the design target. The pink square toroid indicates the detection domain Ω_{det}. The cross-sectional resonator shape is designed in a specified domain on the z-r plane, which is shown as a dotted square.

The sensing mechanism of the WGM biosensor is based on detection of the resonance wavelength or the frequency shift caused by a change in the state of the sensor surface [5]. In the case where the proposed sensor senses a change in state in the specified domain Ω_{det}, the fractional resonant wavelength shift $\delta\lambda$ caused by the average variation of the relative permittivity $\delta\epsilon$ over the detection domain is formulated as a ratio between the variation of the local energy of the detection domain and the total energy of the system [21]:

$$\frac{\delta\lambda}{\lambda} = -\frac{\delta\omega}{\omega} \cong -\frac{\delta\epsilon E_{\text{det}}}{2U} \tag{1}$$

where

$$E_{\text{det}} = \int_{\Omega_{\text{det}}} |\boldsymbol{E}(\boldsymbol{x})|^2 dx \tag{2}$$

$$U = \int_{\Omega} \epsilon(\boldsymbol{x})|\boldsymbol{E}(\boldsymbol{x})|^2 dx \tag{3}$$

where E_{det} is the integral of the square of the electric field intensity over the detection domain, U is the total electrical energy of the system, $\boldsymbol{x}$ is the position in the domain Ω and $\boldsymbol{E}$ and ϵ are the electric field and the relative permittivity at $\boldsymbol{x}$, respectively. According to (1), a higher energy concentration is required in the detection domain Ω_{det} to obtain a larger frequency shift.

(1) can be extended to the criteria representing the permittivity variation detection limit of the test object. Arnold et al. related the smallest measurable frequency shift $\delta\omega_{\min}$ to the half width γ of the resonance frequency ω as: $\delta\omega_{\min} \cong F\gamma$, where F is a specified measurement acuity factor [22]. From the definition of the Q factor, $Q = \omega/\gamma$, $|\delta|_{\min}/\omega \cong F/Q$ is obtained. By substituting this into (1), the smallest measurable relative permittivity change $\delta\epsilon_{\min}$ is represented by:

$$\delta\epsilon_{\min} \cong 2F\frac{U}{E_{\text{det}}Q} \tag{4}$$

Because the numerator of (4) is given when the resonant wavelength is assumed to be fixed, both the integral of the square of the electric field intensity over the detection domain E_{det} and the Q factor should be maximized to minimize $\delta\epsilon_{\min}$.

B. Equations of state of the WGM biosensor

The equations of state of the WGM biosensor form an eigenvalue problem of the 3D vector Helmholtz equations within the domain of the sensor device and its surroundings for calculation of the resonance wavelengths. If the resonator medium is isotropic, then the Helmholtz equation for the magnetic field $\boldsymbol{H}$, as derived from Maxwell's equations, is written as follows:

$$\nabla \times \left(\frac{1}{\epsilon}\nabla \times \boldsymbol{H}\right) - \frac{1}{c^2}\frac{\partial^2 \boldsymbol{H}}{\partial t^2} = 0 \tag{5}$$

where ϵ is the relative permittivity and c is the speed of light. Here, the time harmonic function is assumed to be in the form $\boldsymbol{H}(\boldsymbol{x}, t) = \boldsymbol{H}(\boldsymbol{x})e^{i\omega t}$ and the above equation is solved as an eigenvalue problem by FEM, where $\omega = 2\pi f$ is the angular resonance frequency, given the resonance frequency f. To suppress any spurious modes in the analysis, a weak

penalty term [23] is introduced to yield the following modified equation, as used in [11]:

$$\nabla \times \left(\frac{1}{\epsilon}\nabla \times \boldsymbol{H}\right) - \alpha\nabla\left(\nabla \cdot \boldsymbol{H}\right) + \frac{\omega^2}{c^2}\boldsymbol{H} = 0 \qquad (6)$$

where α is a coefficient. The following two types of boundary conditions are considered for the above equation:

$$\boldsymbol{H} \times \hat{\boldsymbol{n}} = 0 \text{ on } \Gamma_{\text{pmc}} \qquad (7)$$

$$\hat{\boldsymbol{n}} \times \nabla \times \boldsymbol{H} + ik\hat{\boldsymbol{n}} \times \hat{\boldsymbol{n}} \times \boldsymbol{H} = 0 \text{ on } \Gamma_{\text{abc}} \qquad (8)$$

where k is the wave number in free space, and $\hat{\boldsymbol{n}}$ is the unit vector normal to the boundary; the former describes perfect magnetic conduction, and the latter describes first-order absorption on the boundary.

The state variable is the set comprising the time-dependent radial, azimuthal, and axial components of the magnetic field vector $\boldsymbol{H}(\boldsymbol{r}, t)$. We factorize the azimuthal dependence from the variable using the cylindrical coordinate system; i.e.,

$$\boldsymbol{H}(\boldsymbol{r}) = e^{iM\phi}[H_r(r,z), iH_\phi(r,z), H_z(r,z)]^T \qquad (9)$$

where M is the azimuthal mode order.

It should be noted that the azimuthal mode order M is a given parameter in the state equations above. Therefore, an appropriate M must be set in the relationship between the specified wavelength and the device geometry.

C. Analysis method

We solve the eigenvalue problem in (6) by FEM. To perform an iterative numerical optimization based on the FEM results, the target WG eigenmode must be selected automatically from the numerous resulting eigenmodes, including the spurious eigenmodes. The two-step analysis that was proposed in [11] is introduced to specify the target mode during the iterative optimization process. A small closed finite-element model, composed of the device surrounded by a perfect magnetic wall, tends to generate non-spurious modes. First, we solve this model to obtain the eigenfrequency of the target WG mode. This model is referred to as the "closed model" in this paper. Then, we solve for the original model surrounded by perfectly matched layer (PML) domains [24] to calculate the Q factor using the specific target eigenfrequency obtained from the closed model. This second step model is referred to as the "open model". All FEM in this paper are performed using commercial COMSOL Multiphysics software in the same manner as earlier works [11], [24].

To calculate the Q factor, we consider only the radiation loss, for which Q_{rad} is calculated as follows [2]:

$$Q_{\text{rad}} = \frac{\text{Re}(f)}{2\text{Im}(f)} \qquad (10)$$

where $\text{Re}(\cdot)$ and $\text{Im}(\cdot)$ represent the real and imaginary parts of the variable, respectively. In the analysis of a domain surrounded by PML domains, the real part of the frequency represents the total energy of the domain, while the imaginary part represents the rate of energy absorption by the PML domain, *i.e.* the radiation loss (see Chapter 5 in [25]).

We verify the results of our numerical calculation by comparing them with the results obtained using an analytical equation based on spherical resonators, as performed in [24]. The analytical equation for the Q factor including the radiation losses for a spherical resonator is proposed in [26]. We calculated the Q factor from (10) after solving (6) by FEM for the TE mode with resonant wavelengths of 850nm and 1550nm for a silica (relative permittivity $\epsilon = 2.09$) spherical resonator. Because the full components of the electric and magnetic fields are calculated using the Maxwell equation in the axisymmetric domain in (6), the TE mode mentioned in this paper is the quasi-mode where the azimuthal component of the electric field is nearly zero. The sphere diameters are varied from 6μm to 20μm and from 10μm to 24μm for the 850nm and 1550nm resonant wavelengths, respectively. Fig. 2 shows a comparison between the results of the analytical solution and those of the numerical solution. A certain level of agreement was obtained at both resonant wavelengths.

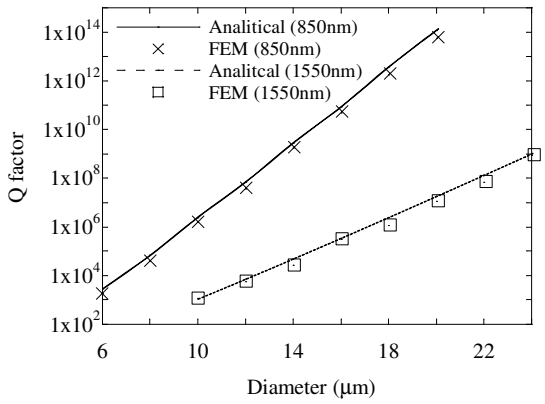

Fig. 2. Comparison between the Q factor values calculated using the analytical equation and FEM.

III. Study of the Cross-Sectional Mode Shapes

Before optimization, we performed several numerical studies of the cross-sectional shape of the WGM biosensor. In general, the cross-sectional shape of the resonator is not modified for a particular sensing target. Here, apart from the practical aspect of manufacturability, we consider the ideal cross-sectional shape for sensing based on the criteria given in (4). In particular, in the case where sensing is performed over a specified domain, such as detection of the density of a liquid, then the most straightforward idea to obtain a strong electric field over the domain is to surround the detection domain by the device. Although such a device shape might increase energy leakage, which in turn leads to a low Q-factor, a higher E_{det} might be promising. Thus, the optimal (i.e. minimum) $\delta\epsilon_{\min}$ in (4) might be obtained using such device shapes. We study this hypothesis numerically. The validity of this numerical study is confirmed using the analytical resonant wavelength shift ratio in (1).

Fig. 3(a) shows the analysis domain for this study. A rectangular-shaped resonator is considered for detection of the relative permittivity variation over the specified domain. The

size of each component is as follows. The air domains of the closed and open models are 1.8μm×3μm and 2.25μm×4μm, respectively. The thickness of the PML domain that surrounds the air domain of the open model is 0.15μm. The inner and outer radii of the square detection domain are labeled rdi and rdo, respectively, as shown in Fig. 3(a). For the square detection domain, two cases are considered: (A): $(rdi, rdo) = (1.0\mu\text{m}, 1.05\mu\text{m})$ and (B): $(rdi, rdo) = (1.0\mu\text{m}, 1.01\mu\text{m})$, with a height of 0.05$\mu$m, when assuming the detection of a homogenous domain state. (B) is considered to be an approximation of the detection on the device surface. The inner and outer radii of the square resonator cross-sections are labeled rri and rro, respectively. The base position of the dielectric is set to be $(rri, rro) = (0.7\mu\text{m}, 1.0\mu\text{m})$, with a height of 0.4$\mu$m. In this base position, the detection domain is located next to the dielectric domain $(rro = rdi)$. The analysis is performed based on the FEM with triangular elements. Second-order Lagrange elements are used for the formulation of each element. The media constituting the resonator and the surrounding domain are assumed to be isotropic GaAlAs with $\epsilon = 11.2896$ and air with $\epsilon = 1$, respectively. The azimuthal mode order M is set to be 10. By considering the case where the incident light has TE polarization, we focused on the first order quasi-TE mode, where the azimuthal component of the electric field is nearly zero, as the study target. Note that, for optimization stability, i.e., where a lower value of M is better for stable analysis during optimization, the device size is assumed to be too small for use as a sensor. For a large M, the solutions to the eigenvalue problem given in (6) contain a large number of spurious modes that interrupt stable optimization. We therefore introduced a relatively small M, which we have already used successfully in our previous research [19]. Let us then suppose that this study can be applied to arbitrarily sized devices.

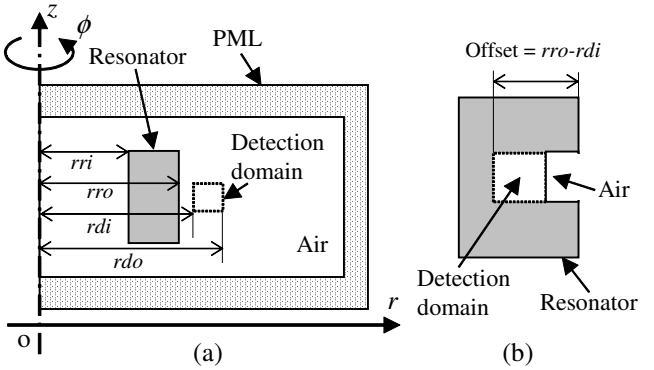

Fig. 3. The analysis domains used in the study of the WGM sensor cross-sectional shape. (a) Model outline. rri and rro are the inner and outer radii of the square resonator cross-sections, respectively. rdi and rdo are the inner and outer radii of the square detection domain, respectively. (b) Overlap shape of the WGM sensor over the detection domain. The offset value is calculated from $rro - rdi$.

We simplify the state change of the detection domain as being a change in the relative permittivity. The relative permittivity of the detection domain is changed from 1 to $1 + 10^{-4}$, assuming the detection of the incorporation of gas in the detection domain. The variation in the resonance wavelength is then calculated according to this change. These calculations are performed for several modified devices. For a fixed detection domain, the device is moved to the r direction to study the overlapped device shape on the detection domain. The overlapped detection domain and its right side domain are regarded as being air, as shown in Fig. 3 (b). This study is performed for $(rri, rro) = (0.7\mu\text{m}, 1.0\mu\text{m})$ (the base position), $(0.75\mu\text{m}, 1.05\mu\text{m})$, $(0.8\mu\text{m}, 1.1\mu\text{m})$, $(0.85\mu\text{m}, 1.15\mu\text{m})$, $(0.9\mu\text{m}, 1.2\mu\text{m})$ and $(0.95\mu\text{m}, 1.25\mu\text{m})$. The offset values between the resonator and the detection domain (see Fig. 3(b)) are 0 (base position), 0.05, 0.1, 0.15, 0.2 and 0.25μm, respectively.

Table I shows the analysis results and contains the Q factor Q_{rad}, the resonance wavelength λ, the square of the electric field intensity of the detection domain $\int_{\Omega_{\text{det}}} |\boldsymbol{E}|^2 dx$, the resonance wavelength change ratios $\delta\lambda/\lambda$ calculated both directly and from analytical equation (1), and the smallest measurable relative permittivity change $\delta\epsilon_{\min}$.

First, the directly calculated resonant wavelength change ratio showed good agreement with the analytical results calculated using (1). Larger offsets caused the Q factor to decrease to a greater degree, because larger slits were set based on the larger offsets, from which the energy leaked. Although the Q factor was reduced, stronger electric fields were obtained in the detection domain up to the 0.15μm offset. At the 0.05μm or 0.1μm offsets, the $\delta\epsilon_{\min}$ values reached their minimum in both the domain (A) and domain (B) cases. This showed that a certain level of overlap between the device and the detection domain certainly reduced $\delta\epsilon_{\min}$. Of course, a lower $\delta\epsilon_{\min}$ was obtained for the case of a wider domain (A).

However, for offsets of more than 0.15μm, E_{det} and $\delta\epsilon_{\min}$ both deteriorated. To enable analysis of the reasons for this behavior, the energy distributions are shown in Fig. 4 for the 0, 0.1 and 0.2μm offsets with detection domain (A). In Fig. 4(a), the energy hot spot is located inside the device. However, the hot spot is located next to the detection domain in Fig. 4(b). This might lead to high electric field intensity in the detection domain. In Fig. 4(c), large grooves divide the mode into two blocks, composed of the upper and lower sides. In this mode, the electric field intensity between the two parts seems to be weak. This mode is therefore inappropriate for sensing purposes, as we confirmed in Table I. The groove size should therefore be adjusted to avoid the mode shown in Fig. 4(c) during the optimization.

IV. Optimization Methodology

A. Topology optimization

The topology optimization is performed based on density or SIMP interpolation schemes, where SIMP stands for solid isotropic material with penalization [13]. The relative permittivity over the design domain is expressed in terms of the density function ρ, $(0 \leq \rho \leq 1)$:

$$\epsilon = \epsilon_{\text{Air}} + \rho(\epsilon_{\text{GaAlAs}} - \epsilon_{\text{Air}}). \tag{11}$$

The optimum cross-sectional shape of the device can then be specified as a distribution in ρ.

TABLE I
RESONANCE WAVELENGTH SHIFT ANALYSIS RESULTS FOR (A) SQUARE AND (B) THIN DETECTION DOMAINS. THE RELATIVE PERMITTIVITY OF THE DETECTION DOMAIN CHANGES FROM 1 TO $1 + 10^{-4}$.

	Offset (μm)	0	0.05	0.1	0.15	0.2	0.25
	Q_{rad}	2.13×10^6	1.29×10^6	7.18×10^5	3.57×10^5	7.20×10^4	2.49×10^4
	λ (nm)	1349	1354	1355	1335	1336	1309
(A)	$\delta\lambda/\lambda$	6.16×10^{-8}	3.42×10^{-7}	6.14×10^{-7}	7.93×10^{-7}	2.12×10^{-7}	1.42×10^{-7}
	$E_{\text{det}}/2U$	6.18×10^{-8}	3.44×10^{-7}	6.15×10^{-7}	7.93×10^{-7}	2.14×10^{-7}	1.45×10^{-7}
	E_{det} (V^{2}m)	4.08×10^{-7}	1.86×10^{-6}	3.06×10^{-6}	3.91×10^{-6}	1.61×10^{-6}	2.33×10^{-6}
	$\delta\epsilon_{\min}$ $(\times 2F)$	3.80×10^{-4}	1.13×10^{-4}	1.13×10^{-4}	1.77×10^{-4}	3.24×10^{-3}	1.39×10^{-2}
(B)	$\delta\lambda/\lambda$	2.07×10^{-8}	7.75×10^{-7}	1.19×10^{-7}	1.48×10^{-7}	7.26×10^{-8}	3.74×10^{-8}
	$E_{\text{det}}/2U$	2.08×10^{-8}	7.78×10^{-8}	1.19×10^{-7}	1.48×10^{-7}	7.34×10^{-8}	3.82×10^{-8}
	E_{det} (V^{2}m)	1.36×10^{-7}	4.14×10^{-7}	5.79×10^{-7}	7.14×10^{-7}	5.32×10^{-7}	5.94×10^{-7}
	$\delta\epsilon_{\min}$ $(\times 2F)$	1.14×10^{-3}	5.06×10^{-4}	5.97×10^{-4}	9.68×10^{-4}	9.80×10^{-3}	5.44×10^{-2}

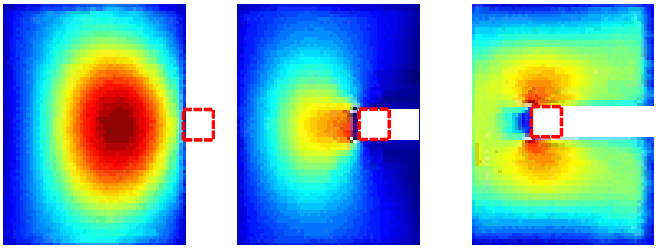

(a) (b) (c)

Fig. 4. Energy distributions of the first TE mode with (a) no offset shape, (b) a 0.1μm offset shape, and (c) a 0.2μm offset shape in the resonator. Red dotted squares indicate the detection domain. The white areas indicate air.

According to our study in Section III, we target the following tasks during optimization to increase the sensitivity of the WGM sensor:

1) Maximization of the integral of the square of the electric field intensity over the detection domain.
2) Maximization of the Q factor associated with the emissions as expressed by (10).
3) Specification of the emission wavelength $\lambda = c/\text{Re}(f)$.

For Task 1, the basic purpose of the optimization process is to increase the electric field intensity in the detection domain. However, to avoid the split mode shown in Fig. 4(c), the energy concentration in the domain adjacent to the detection domain should also be considered as part of the optimization process. Let us set the domain Ω_{ec} for the energy concentration on the left side of the detection domain, as shown in Fig. 5. Unlike the detection domain Ω_{det}, Ω_{ec} is included within the design domain. Task 3 is then assumed to be satisfied by introducing a corresponding equality constraint. In the eigenfrequency analysis, assuming the normalized eigenmodes $\boldsymbol{H}$ ($\int_\Omega |\boldsymbol{H}|^2 dx = 1$), the total electric energy over the analysis domain is equal to the square of the angular eigenfrequency ($\int_\Omega \epsilon |\boldsymbol{E}|^2 dx = \text{Re}(\omega)^2$) [27]. This means that, by prespecifying the emission wavelength and the azimuthal mode order, the numerator in the expression for the Q-factor remains constant during optimization. Thus, the objective functions for Task 1, J_E, and Task 2, J_Q, and the equality constraint h for Task 3 are formulated as follows:

$$\underset{\rho}{\text{minimize}}\, J_E(\rho) = -\int_{\Omega_{\text{det}}} |\boldsymbol{E}|^2 dx - \int_{\Omega_{\text{ec}}} \epsilon |\boldsymbol{E}|^2 dx \tag{12}$$

or/and

$$\underset{\rho}{\text{minimize}}\, J_Q(\rho) = \text{Im}(f) \tag{13}$$

subject to

$$h(\rho) = \lambda - \lambda_0 = 0 \tag{14}$$

where λ_0 denotes the specified wavelength. Based on the above formulation, an optimal WGM sensor geometry under fixed azimuthal order and emission wavelength conditions is obtained.

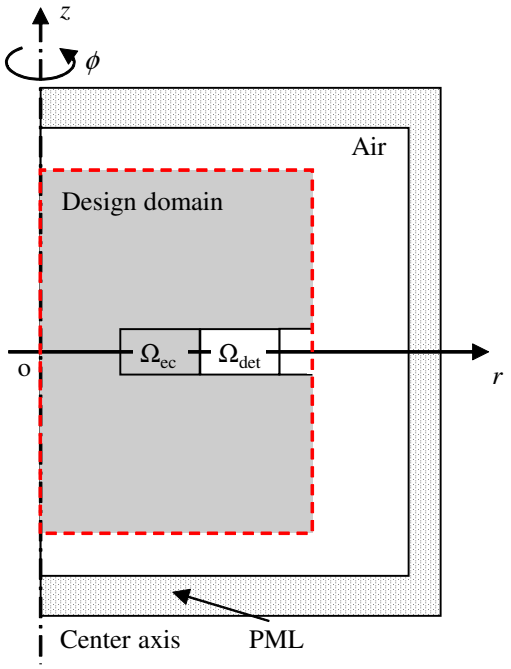

Fig. 5. Outline of the analysis model used in the optimization process. The gray domains indicate the design domain. The red dotted square indicates the domain used to display the optimal configuration in the numerical examples.

B. Numerical implementation and optimization algorithm

The massive scale of the optimization problem means that the density function must usually be updated using gradient-based algorithms, and the sensitivities for both objective functions and the constraint must be calculated. The sensitivity of the objective function in (13) can be expressed in terms of the functions of the state variable and its adjoint. Because the electric field $\boldsymbol{E}$ is calculated as an eigenmode of the eigenvalue problem, the sensitivity and the adjoint equation are formulated using the expression for the eigenmode studied in [28]. The sensitivity of the objective function in (13) and of the equality constraint in (14) can be calculated from state variables only, without solving the adjoint equation, because the optimization problem of the eigenfrequency is a self-adjoint problem [29].

During the optimization process, the first order eigenmode shape can be switched in the eigenvalue problem. In the case of this optimization problem, the orders of the eigenmodes shown in Fig. 4(b) and (c) can be switched. To continue to track the target eigenmode, we solve the eigenmode problem by using a closed model for several eigenvalues. We then specify the target eigenvalue by evaluating the least square error between the target eigenmode of the previous iteration and several eigenmodes obtained from the current iteration. The eigenmode with the lowest error is chosen as the target of the current iteration.

Fig. 6 shows a flowchart of the optimization procedure. First, the closed model is solved by FEM to find the eigenfrequency of the target WG mode. Second, the original open model is solved by FEM, and the objective function and the constraint are calculated. Sensitivities for both the objective function and the constraint must also be calculated. Next, the adjoint equation is solved by FEM and the sensitivities of the objective function and the constraint are calculated. Finally, the density functions are updated by using the phase field method [20] which is a boundary variation methodology based on the density function. Topology optimization processes sometimes encounter problems related to gray unclear domains. It is difficult to identify whether these domains belong to the optimal shape or the void. Thus, the phase field method, which is free of the gray domain problem, is used. These procedures are repeated until the iteration limit is reached or until certain specified convergence criteria hold. The converged optimal solutions are post-processed by thresholding of the density function with a value of 0.5 to obtain clear black-and-white shapes. In our previous work, the performance change caused by this thresholding process was not too large to interrupt a relative comparison of each of the optimal solutions [30].

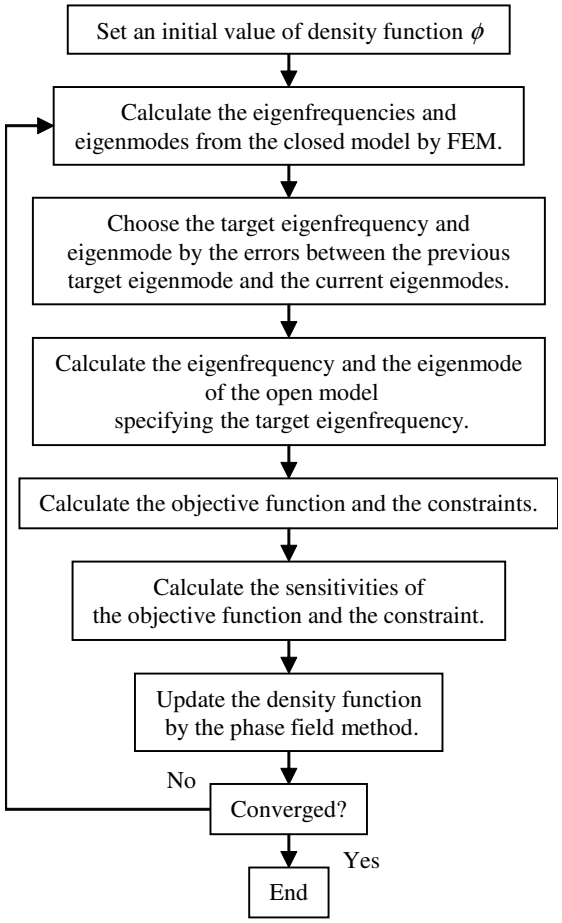

Fig. 6. Flowchart of the optimization procedure.

V. Numerical examples

Some numerical examples are studied based on the optimal shape of the WGM sensor using the proposed methodology. The optimization processes are performed using the same specified quasi-TE modes as those used in the studies in Sections II and III, where the azimuthal component of the electric field is nearly zero for $M = 10$. The material data, the size of the air space and the PML are also the same. The size of the detection domain Ω_{det} is set in each example. The domain Ω_{ec} for the energy concentration in the device is set next to the left side of Ω_{det} with a square shape with 0.04μm sides. The design domain is 1.5μm$\times$2μm. This domain is meshed using triangular elements. Second-order Lagrange elements are used for the formulation of each element. The density function is discretized as a piecewise-constant function in the design domain by a 75$\times$100 square mesh. By assuming horizontal mirror symmetry for the optimal shapes, only the upper half of the design domain is optimized. Thus, 7500 design variables are updated during the optimization process in this problem. All optimizations are performed with a specified wavelength $\lambda_0 = 1300$nm, assuming that the input is from an InGaAsP/InP laser.

A. Optimization for high electric field intensity in the detection domain

The first optimization is performed to improve the electric field intensity at the specified detection domain by using the objective function in (12). The detection domain is set to be the same as domain (A) in the study in Section III, where $(rdi, rdo) = (1.0\mu\text{m}, 1.05\mu\text{m})$ in Fig. 1(a). Fig. 7 shows the convergence history of the objective function and the resonance wavelength up to 40 iterations. A smooth convergence was obtained, satisfying the constraint. Fig. 8(a) shows

the optimal configuration obtained at iteration 39, shown in 1.5μm$\times 2\mu$m boxes that were indicated by the red dotted square in Fig. 5, where the left side of the figure corresponds to the center axis. The distributions of the electric energy density $\epsilon|E|^2$ and the electric field intensity $|E|^2$ are shown in Fig. 8(a) and (b). The small squares shown in Fig. 8(a) and (b) represent the detection domain Ω_{det} and the energy concentration domain Ω_{ec}. Both domains are shown side by side in each figure; however, one of them is less visible because of the surrounding colors in Fig. 8(a) and (b). The resulting E_{det} and Q factor are $E_{\text{det}} = 1.03 \times 10^{-5}$ and $Q_{\text{rad}} = 1.36 \times 10^{5}$, respectively. The optimal shape is concave near the energy concentration domain to enhance the maximum electric energy. As a result, a strong electric field can be observed in the detection domain. This shape is very similar to the optimal shape for minimization of the mode volume reported in [19].

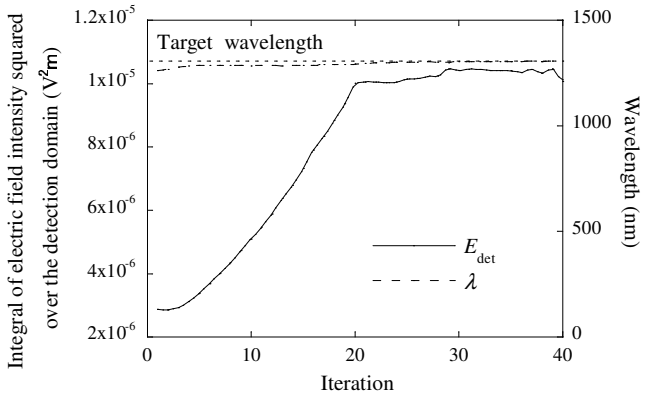

Fig. 7. Convergence history of the integral of the square of the electric field intensity over the detection domain E_{det} and the wavelength.

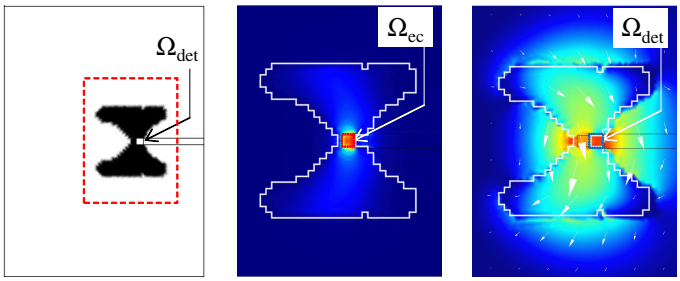

Fig. 8. (a) Optimal shape shown in the domain represented by the red dotted square in Fig. 5. The outline of the optimal shape is also shown in (b) and (c) as a white line. (b) The electric energy density $\epsilon|E|^2$ distribution shown inside the red dotted line domain of (a). The red dotted square indicates the energy concentration domain. (c) Logarithmic electric field intensity $|E|^2$ distribution shown inside the red dotted line domain of (a), where the white arrows indicate the magnitude and direction of the electric field in the medial plane. The blue dotted square indicates the detection domain.

B. Study of size effect of detection domain on optimization results.

The optimization processes for the electric field intensity of the detection domain are performed for several detection domain sizes. First, the detection domain width is changed from that of the first optimization example. The inner radius and the height remain fixed. The domain width is changed from 0.05μm to 0.01μm and 0.1μm. Fig. 9 shows the optimal configurations for both optimizations. The shapes of the device centers were different for the different detection domain widths. For the wide detection domain, a deep groove was generated. Table II shows a summary of the performance criteria for the optimal results. Higher electric field intensities were obtained for the larger detection domains. However, the Q factors decreased in the case of the 0.1μm detection domain width, because a large device surface area was exposed near the energy hot spot. (Q was slightly higher in the 0.05μm domain than in the 0.01μm domain, and this might have been caused by an optimization error that occurred in the black-and-white post-processing step. Before this process, the result for the 0.01μm domain was actually approximately 26% higher for Q than that in the 0.05μm domain.) Comparison of $E_{\text{det}} \times Q_{\text{rad}}$, which is the denominator of $\delta\epsilon_{\min}$, among these three cases shows that larger detection domains lead to increases in $E_{\text{det}} \times Q_{\text{rad}}$, although expansion of the detection domain in turn reduces the Q factor.

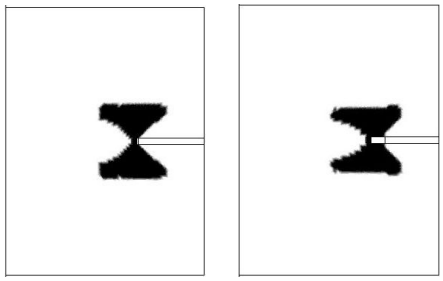

Fig. 9. Optimal shapes for (a) 0.01μm and (b) 0.05μm detection domain widths.

TABLE II
SUMMARY OF E_{det} AND Q FACTOR RESULTS FROM THE OPTIMIZATION PROCESS FOR THREE DIFFERENT DETECTION DOMAIN WIDTHS.

Height of Ω_{det} (μm)	E_{det} (V^{2}m)	Q_{rad}	$E_{\text{det}} \times Q_{\text{rad}}$ (V^{2}m)
0.01	1.82×10^{-6}	1.22×10^{5}	0.22
0.05	1.03×10^{-5}	1.36×10^{5}	1.40
0.1	2.61×10^{-5}	6.49×10^{4}	1.69

Next, the detection domain height is changed with fixed values for the inner and outer radii. The domain height is changed from 0.05μm to 0.1μ and 0.2μm. Fig. 10 shows the optimal configurations for both optimizations. The optimization process worked well even for vertically long detection domains. Table III shows a summary of the performance criteria for the optimal results. Higher electric field intensities and lower Q factors were obtained for larger detection domains for the same reasons as in the previous example. The same can be said to apply to $E_{\text{det}} \times Q_{\text{rad}}$.

To summarize this example, the proposed methodology works well for an arbitrary detection domain size, and larger

detection domain sizes lead to increased $E_{\text{det}} \times Q_{\text{rad}}$ values, although the Q factor is reduced by the increase in energy leakage.

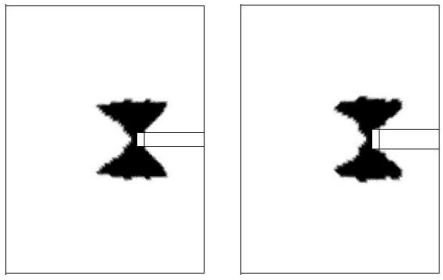

(a) (b)

Fig. 10. Optimal shapes for (a) 0.1μm and (b) 0.15μm high detection domains.

TABLE III
SUMMARY OF E_{det} AND Q FACTOR RESULTS FROM THE OPTIMIZATION PROCESS FOR THREE DIFFERENT DETECTION DOMAIN HEIGHTS.

Height of Ω_{det} (μm)	E_{det} (V^{2}m)	Q_{rad}	$E_{\text{det}} \times Q_{\text{rad}}$ (V^{2}m)
0.05	1.03×10^{-5}	1.36×10^{5}	1.40
0.1	2.27×10^{-5}	1.03×10^{5}	2.34
0.15	3.18×10^{-5}	8.05×10^{4}	2.56

C. Study of effect of detection domain location on optimization results.

The location of the detection domain is also an important factor that could seriously affect the sensor performance, because the analysis and optimization are performed in the cylindrical coordinate system. The right-and-left locations of the detection domain could decide the radius of the WGM sensor. While maintaining the cross-sectional size of the detection domain at 0.05μm$\times$0.05μm, which is the size set in the first example, the inner radius rdi in Fig. 3 (a) is set to 0.85μm and 1.15μm. The results for these values are compared with the results of the first example where rdi=1.0μm. Fig. 11 shows the optimal configurations for both optimizations. Table IV shows a summary of the performance criteria for these optimal results. Under a fixed wavelength and azimuthal order, the cross-section size of the WGM sensor decreased as the radius of the device increased, as reported in [19]. In the experiments, the Q factor generally increases as the device radius increases under illumination from a fixed light source, because the number of light waves (the azimuthal order M in (9)) and the stored energy increase. However, under the conditions with the fixed azimuthal order and emission wavelength used for this optimization in our numerical study, the stored energy is nearly fixed despite the increase in the device radius. Because the energy loss increases with increments in the device radius, the Q factor decreases. Thus, the relationships between the device radius and Q factor in the general experiments and in our numerical studies were different. In addition, because the energy hot spot is exposed to the detection domain, this effect could be serious for this particular problem. E_{det} increases with increases in the inner radius. This is simply because the integration volume was increased when the detection domain moved outward. However, because the reduction in the Q factor was steeper than this increase, a larger $E_{\text{det}} \times Q_{\text{rad}}$ value was obtained in the inner location of the detection domain.

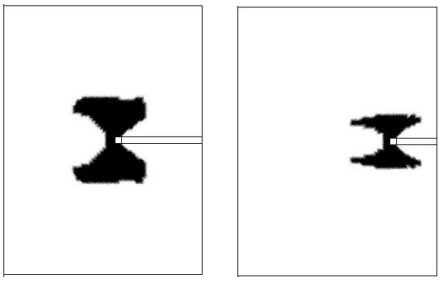

(a) (b)

Fig. 11. Optimal shapes for (a) 0.85μm and (b) 0.115μm inner radius detection domains.

TABLE IV
SUMMARY OF E_{det} AND Q FACTOR RESULTS FROM THE OPTIMIZATION PROCESS FOR THREE DIFFERENT DETECTION DOMAIN POSITIONS.

Inner radius of Ω_{det} (μm)	E_{det} (V^{2}m)	Q_{rad}	$E_{\text{det}} \times Q_{\text{rad}}$ (V^{2}m)
0.85	6.30×10^{-6}	6.35×10^{5}	4.00
1.0	1.03×10^{-5}	1.36×10^{5}	1.40
1.15	1.26×10^{-5}	1.06×10^{4}	0.13

D. Simultaneous optimization of E_{det} and the Q factor.

Before direct optimization of $E_{\text{det}} \times Q_{\text{rad}}$, simultaneous optimization of E_{det} and Q_{rad} is performed using a weighting coefficient method. The relationship between E_{det} and Q_{rad} under the same optimization conditions could be identified via this study. The following objective function is introduced by integrating (12) and (13) using the weighting factor w $(0 \leq w \leq 1)$:

$$\underset{\rho}{\text{minimize}}\, J(\rho) = -w * \left(\int_{\Omega_{\text{det}}} |\boldsymbol{E}|^2 dx + \int_{\Omega_{\text{ec}}} \epsilon |\boldsymbol{E}|^2 dx \right) + (1-w) * \text{Im}(f) \tag{15}$$

The detection domain is set to be the same as domain (A) in the study in Section III, where $(rdi, rdo) = (1.0\mu\text{m}, 1.05\mu\text{m})$ in Fig. 3 (a). By varying the weighting coefficient from 0 to 1, five optimal results are found; see Fig. 12. Result (a) corresponds to that shown in Fig. 8. A trade-off relationship between the electric field intensity and the Q-factor can be seen in these results, i.e., where a larger electric field intensity must lead to a lower Q factor and vice versa, given the same wavelength and azimuthal mode order conditions. The characteristics of these shapes can be found by analysis of the energy distribution. In Fig. 12 (b), a similar energy distribution to that of result (a) can be obtained, because the Q factor term

in the objective function was weaker. In Fig. 12 (c), although the energy hot spot is next to the detection domain, relatively high energy concentrations can be observed in both the upper and lower sides of the cross-section. In Fig. 12 (d) and (e), the hot spot moved away from the detection domain to reduce the energy losses. The dielectric is connected between the hot spot and the detection domain to transfer the electric energy. These results show that an optimization process to produce both high electric field intensity and a high Q factor could be performed using the proposed methodology. Table V shows a summary of the performance criteria for these optimal results. Optimal shape (d) has the largest value for $E_{\text{det}} \times Q_{\text{rad}}$.

Finally, direct optimization of $E_{\text{det}} \times Q_{\text{rad}}$ is performed under the same conditions that were used in Section V-D. According to (4), $\delta\epsilon_{\min}$ is minimized by maximizing E_{det} and the Q factor at a fixed resonant frequency. In this case, the numerator of (10) is also fixed. Thus, the variable of $E_{\text{det}} \times Q_{\text{rad}}$ during the optimization is $E_{\text{det}}/\text{Im}(f)$. Based on this, the following objective function is introduced by integrating (12) and (13):

$$\underset{\rho}{\text{minimize}}\, J(\rho) = \frac{\int_{\Omega_{\text{det}}} |\boldsymbol{E}|^2 dx + \int_{\Omega_{\text{ec}}} \epsilon |\boldsymbol{E}|^2 dx}{\text{Im}(f)} \tag{16}$$

Fig. 13 shows the optimal configuration, the distribution of the electric energy density $\epsilon|E|^2$ and the electric field intensity $|E|^2$. This optimal shape has a shape similar to optimal shape (d) in Fig. 12. These results were also shown in Fig. 12 and Table V along with the previous results. The largest $E_{\text{det}} \times Q_{\text{rad}}$ value was certainly obtained via this study.

TABLE V
SUMMARY OF RESULTS OF SIMULTANEOUS OPTIMIZATION OF E_{det} AND Q FACTOR.

Fig. No.		w in (15)	E_{det} (V^2m)	Q_{rad}	$E_{\text{det}} \times Q_{\text{rad}}$ (V^2m)
Figs. 8 and 12	(a)	1.00	1.03×10^{-5}	1.36×10^{5}	1.40
Fig. 12	(b)	0.05	4.63×10^{-6}	1.49×10^{5}	0.69
	(c)	0.025	2.56×10^{-6}	3.01×10^{5}	0.77
	(d)	0.01	1.99×10^{-6}	1.40×10^{6}	2.79
	(e)	0.005	6.35×10^{-7}	1.93×10^{6}	1.22
Fig. 13	(a)	-	3.63×10^{-6}	1.09×10^{6}	3.96

VI. CONCLUSION

In this research, we studied and identified optimal shapes for WGM micro-ring sensors with high detection sensitivity. As criteria for the high sensitivity characteristics of the WGM sensor, we defined the smallest measurable relative permittivity change that was calculated from the integral of the square of the electric field over the detection domain and the Q factor. Our systematic procedure helps us to find optimal device shapes with specifically-designed performance levels given a prescribed emission wavelength and WG resonance mode. As a basic principle for WGM sensor design, we found that concave shapes produced high electric field intensities near the cross-sectional centers of the devices. We confirmed several relationships between the detection domain size and location and the sensor performance. Larger detection domains were likely to lead to better smallest measurable relative permittivity values, although the corresponding Q factors decrease because of the increased energy leakage. As a result, the optimum device was found to have a small radius, a large detection domain and a concave shape with its center located next to the detection domain with its prescribed emission wavelength and WGM azimuthal order. We also succeeded in direct optimization of the sensor sensitivity by considering both the integral of the square of the electric field intensity over the detection domain and the Q factor. When we consider sensor manufacturability, the concave shape might prove impractical. Although the shape itself is formed by step-by-step lamination, it may be very costly to manufacture. However, the fundamental findings that we have obtained from the optimization process performed here will enable improved practical shape design, such as a spherical resonator with a small groove, in our future work.

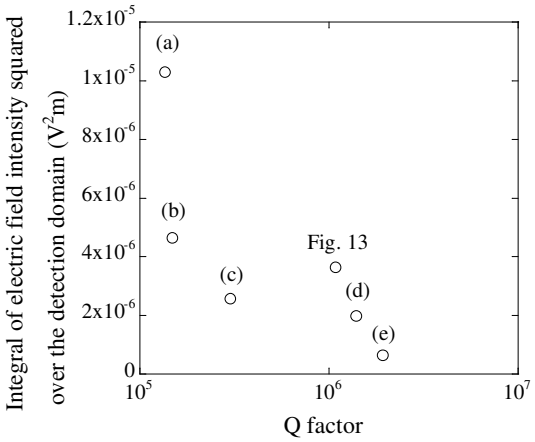

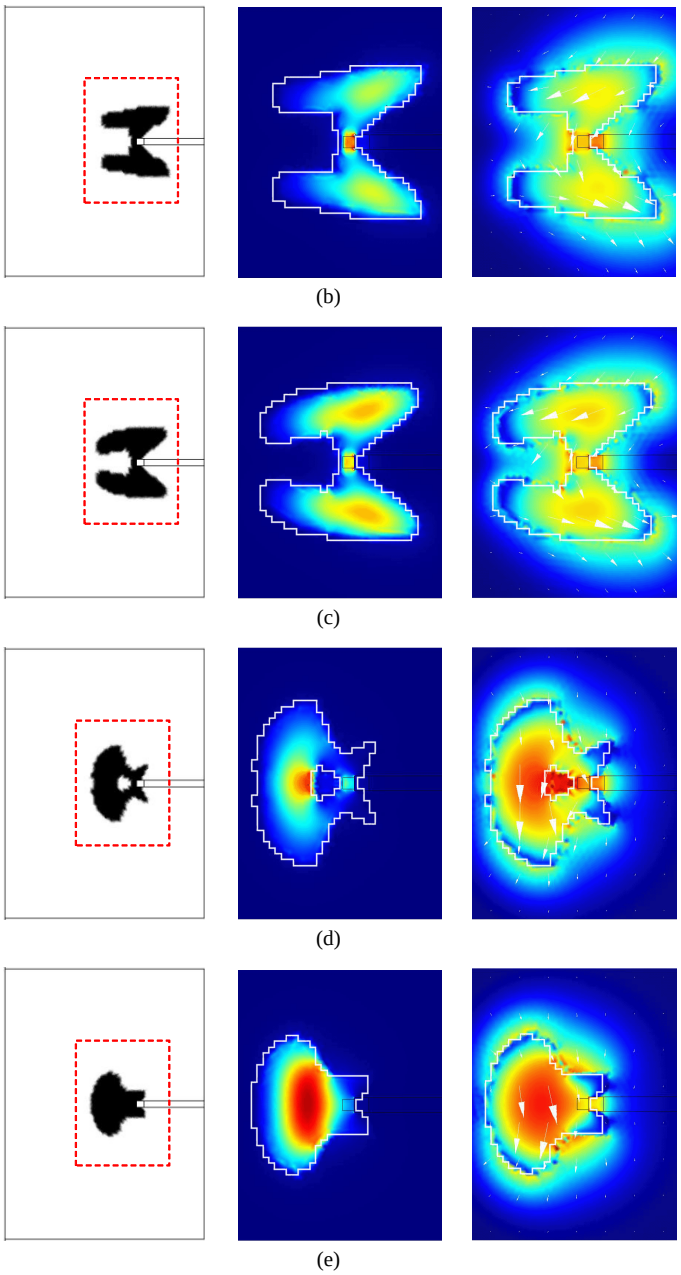

Fig. 12. Optimal results obtained by maximizing E_{det} and the Q factor using different weighting factor settings in (15). The left figure shows the optimal configuration. The figures in the center and on the right show the energy distribution and the logarithmic electric field intensity distribution within the red dotted line domain of the left figure corresponding to each setting. The white lines indicate the outlines of the optimal shape.

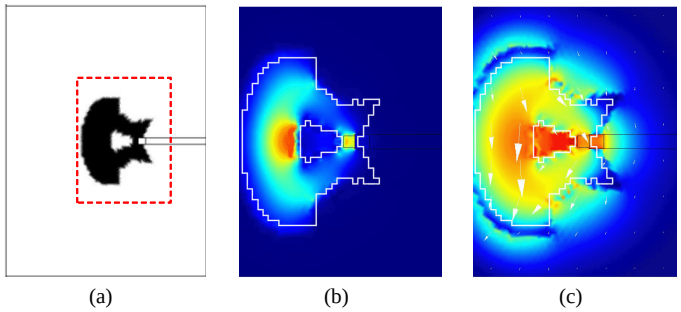

Fig. 13. Optimal results obtained by maximizing both E_{det} and the Q_{rad} in (16). Part (a) shows the optimal configuration. Parts (b) and (c) show the energy distribution and the logarithmic electric field intensity distribution within the red dotted line domain of (a) corresponding to each setting. The white lines indicate the outlines of the optimal shape.

REFERENCES

[1] K. J. Vahala, "Optical microcavities," *Nature*, vol. 424, pp. 839–846, 2003.

[2] A. Oraevsky, "Whispering-gallery waves," *Quant. Electron.*, vol. 32, no. 5, pp. 377–400, 2002.

[3] F. Vollmer, D. Braun, A. Libchaber, M. Khoshsima, I. Teraoka, and S. Arnold, "Protein detection by optical shift of a resonant microcavity," *Appl. Phys. Lett.*, vol. 80, no. 21, pp. 4057–4059, 2002.

[4] A. M. Armani and K. J. Vahala, "Heavy water detection using ultra-high-q microcavities," *Opt. Lett.*, vol. 31, no. 12, pp. 1896–1898, 2006.

[5] F. Vollmer and S. Arnold, "Whispering-gallery-mode biosensing: label-free detection down to single molecules," *Nature methods*, vol. 5, no. 7, pp. 591–596, 2008.

[6] T. Ioppolo, N. Das, and M. V. Otugen, "Whispering gallery modes of microspheres in the presence of a changing surrounding medium: A new ray-tracing analysis and sensor experiment," *J. App. Phys.*, vol. 107, no. 10, 103105, 2010.

[7] Q. Ma, T. Rossmann, and Z. Guo, "Temperature sensitivity of silica micro-resonators," *J. Phys. D: Appl. Phys.*, vol. 41, no. 24, 245111, 2008.

[8] T. Ioppolo, M. Kozhevnikov, V. Stepaniuk, M. V. Ötügen, and V. Sheverev, "Micro-optical force sensor concept based on whispering gallery mode resonators," *Appl. Opt.*, vol. 47, no. 16, pp. 3009–3014, 2008.

[9] T. Ioppolo and M. V. Ötügen, "Pressure tuning of whispering gallery mode resonators," *J. Opt. Soc. Am. B*, vol. 24, no. 10, pp. 2721–2726, 2007.

[10] N. Q. Nguyen, N. Gupta, T. Ioppolo, and M. V. Ötügen, "Whispering gallery mode-based micro-optical sensors for structural health monitoring of composite materials," *J. Mater. Sci.*, vol. 44, no. 6, pp. 1560–1571, 2009.

[11] M. Oxborrow, "Traceable 2-d finite-element simulation of the whispering-gallery modes of axisymmetric electromagnetic resonators," *IEEE Trans. Microw. Theor. Tech.*, vol. 55, no. 6, pp. 1209–1218, 2007.

[12] H. Quan and Z. Guo, "Simulation of whispering-gallery-mode resonance shifts for optical miniature biosensors," *J. Quant. Spectrosc. Radiat. Transfer*, vol. 93, no. 1, pp. 231–243, 2005.

[13] M. P. Bendsøe and O. Sigmund, *Topology Optimization: Theory, Methods, and Applications*. Berlin: Springer-Verlag, 2003.

[14] J. Jensen and O. Sigmund, "Systematic design of photonic crystal structures using topology optimization: Low-loss waveguide bends," *Appl. Phys. Lett.*, vol. 84, no. 12, pp. 2022–2024, 2004.

[15] W. R. Frei, D. A. Tortorelli, and H. T. Johnson, "Topology optimization of a photonic crystal waveguide termination to maximize directional emission," *Appl. Phys. Lett.*, vol. 86, 111114, 2005.

[16] J. Andkjær, S. Nishiwaki, T. Nomura, and O. Sigmund, "Topology optimization of grating couplers for the efficient excitation of surface plasmons," *J. Opt. Soc. Am. B*, vol. 27, no. 9, pp. 1828–1832, 2010.

[17] A. R. Diaz and O. Sigmund, "A topology optimization method for design of negative permeability metamaterials," *Struct. Multidisc. Optim.*, vol. 41, no. 2, pp. 163–177, 2010.

[18] J. Andkjær and O. Sigmund, "Topology optimized low-contrast all-dielectric optical cloak," *Appl. Phys. Lett.*, vol. 98, no. 2, 021112, 2011.

[19] A. Takezawa and M. Kitamura, "Cross-sectional shape optimization of whispering-gallery ring resonators," *IEEE/OSA J. Lightwave Tech.*, vol. 30, no. 17, pp. 2776–2782, 2012.

[20] A. Takezawa, S. Nishiwaki, and M. Kitamura, "Shape and topology optimization based on the phasefield method and sensitivity analysis," *J. Comput. Phys.*, vol. 229, no. 7, pp. 2697–2718, 2010.

[21] S. Arnold, M. Khoshsima, I. Teraoka, S. Holler, and F. Vollmer, "Shift of whispering-gallery modes in microspheres by protein adsorption," *Opt. Lett.*, vol. 28, no. 4, pp. 272–274, 2003.

[22] S. Arnold, R. Ramjit, D. Keng, V. Kolchenko, and I. Teraoka, "Microparticle photophysics illuminates viral bio-sensing," *Faraday Discuss.*, vol. 137, pp. 65–83, 2008.

[23] M. Koshiba, K. Hayata, and M. Suzuki, "Improved finite-element formulation in terms of the magnetic field vector for dielectric waveguides," *IEEE Trans. Microw. Theor. Tech.*, vol. 33, no. 3, pp. 227–233, 1985.

[24] M. I. Cheema and A. G. Kirk, "Accurate determination of the quality factor and tunneling distance of axisymmetric resonators for biosensing applications," *Opt. Express*, vol. 21, no. 7, pp. 8724–8735, 2013.

[25] D. W. Prather, S. Shi, A. Sharkawy, J. Murakowski, and G. J. Schneider, *Photonic Crystals, Theory, Applications and Fabrication*. Hoboken: Wiley, 2009.

[26] V. V. Datsyuk, "Some characteristics of resonant electromagnetic modes in a dielectric sphere," *Appl. Phys. B*, vol. 54, no. 2, pp. 184–187, 1992.

[27] G. Allaire, *Numerical Analysis and Optimization: An Introduction to Mathematical Modelling and Numerical Simulation*. Oxford University Press, 2007.

[28] A. Takezawa and M. Kitamura, "Sensitivity analysis and optimization of vibration modes in continuum systems," *J. Sound Vib.*, vol. 332, pp. 1553–1566, 2013.

[29] E. J. Haug, K. K. Choi, and V. Komkov, *Design Sensitivity Analysis of Structural Systems*. Orlando: Academic Press, 1986.

[30] A. Takezawa and M. Kitamura, "Phase field method to optimize dielectric devices for electromagnetic wave propagation," *J. Comput. Phys.*, vol. 257PA, pp. 216–240, 2014.

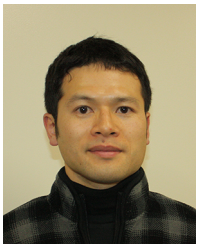

Akihiro Takezawa Akihiro Takezawa earned his Bachelor of Engineering Degree in Precision Engineering from Kyoto University in 2003 and his Master's Degree in Precision Engineering from Kyoto University in 2005. He also received his Doctor of Philosophy Degree in Precision Engineering from Kyoto University in 2009. He is now an Associate Professor in the Institute of Engineering at Hiroshima University.

Masanobu Haraguchi Masanobu Haraguchi earned his Bachelor of Engineering Degree in Electronic Engineering from Osaka University in 1985 and his Master's Degree in Electronic Engineering from Osaka University in 1987. He also received his Doctor of Philosophy Degree in Electronic Engineering from Osaka University in 1993. He is now a Professor in the Institute of Technology and Science at the University of Tokushima.

Toshihiro Okamoto Toshihiro Okamoto earned his Bachelor of Engineering Degree in Electronic Engineering from the University of Tokushima in 1991 and his Master's Degree in Electronic Engineering from the University of Tokushima in 1993. He also received his Doctor of Philosophy Degree in Electronic Engineering from the University of Tokushima in 2000. He is now an Assistant Professor in the Institute of Technology and Science at the University of Tokushima.

Mitsuru Kitamura Mitsuru Kitamura earned his Bachelor of Engineering Degree in Civil Engineering from Tokyo Metropolitan University in 1980 and his Master's Degree in Engineering Mechanics from Ohio State University in 1982. He also received his Doctor of Philosophy Degree in Engineering Mechanics from Ohio State University in 1987. He is now a Professor in the Institute of Engineering at Hiroshima University.